Multi-Pass Automotive Synthetic Aperture Radar Image Fusion

Jason M. Merlo and Jeffrey A. Nanzer

Department of Electrical and Computer Engineering, Michigan State University

{merlojas, nanzer}@msu.edu

Abstract—In this work we demonstrate an efficient technique for the registration and compositing of multiple automotive synthetic aperture radar (SAR) images as a step towards distributed SAR imaging. Through the use of an efficient sub-pixel Fourier-based iterative correlation and refinement technique, sub-sections of the overall SAR images are aligned. Because only small sub-regions of the full SAR images are aligned at a time, this technique inherently compensates for accelerations experienced when sampling the synthetic aperture, by assuming a quasi-constant velocity over small sub-regions of the image. Because the image fusion is performed after image formation, this technique lends itself well to a distributed architecture where the image formation is performed on-vehicle and transferred to other vehicles or a centralized cloud processor where images from other vehicles can be aggregated. Finally, because the registration of sub-regions of the SAR images are performed, the registration alignment vector can be used as a odometry provider to improve vehicle odometry estimates; if a metrology grade SAR map is used as reference, a globally reference position estimate could be performed.

I. Introduction

In recent years, vehicles have been rapidly approaching levels 3 and 4 of autonomy [1], with advanced driver assistance features beginning to approach the level of reliability sought for truly hands-free driving. At the same time, vehicle connectivity is also increasing with vehicle-to-vehicle (V2V) and vehicle-to-infrastructure (V2I) equipment being added to share safety information such as road hazards detected and traffic light state. However, to reach the high levels of automation defined in level 4 standards, vehicles will need to be able to operate sufficiently autonomously that they can maintain a sufficient level of occupant safety in all operating scenarios in their operational design domain (ODD). Recently, several examples of commercial level 4 vehicles have entered the market with limited ODDs, however these rely on sophisticated suites with many bespoke, high-performance sensors and powerful in-vehicle compute servers, which can exceed the cost of the vehicle itself. To bridge the gap between the highly automated level 3 technologies available in consumer vehicles today and those of fully automated level 4 vehicles, dramatic reductions in sensing and compute costs must be achieved. One approach towards this goal is to leverage the information already available in the level 3 sensor suite to a fuller extent; typically, an array of advanced multiple-input multiple-output (MIMO) radars are available on all sides of an automated vehicle allowing for long-range perception of
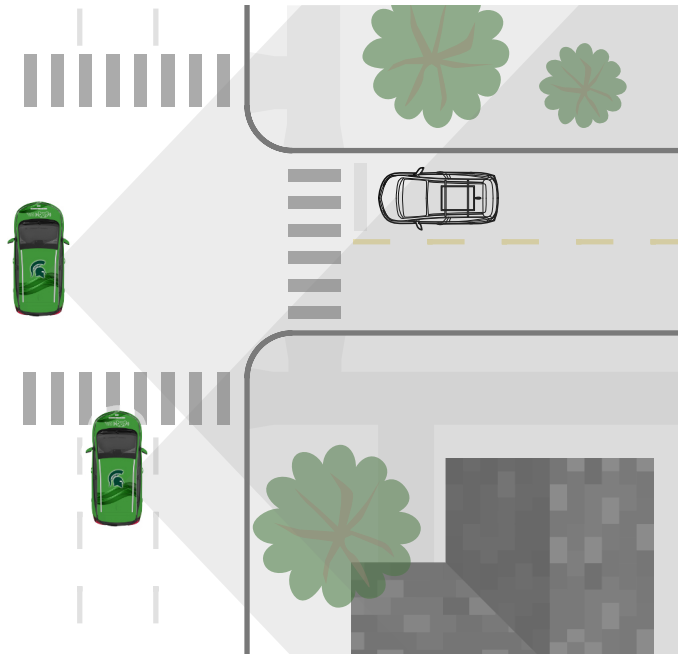

Fig. 1. Conceptual image of multi-pass automotive SAR. Separate vehicles collect SAR data which is then fused to improve spatial diversity and angular resolution.

vehicles, vulnerable road users, and road hazards in all weather conditions. However, these sensors often suffer from poor angular resolution due to the limitations in device aperture sizes practical for low-cost production. To compensate for this, lidar sensors are often used, however these are typically significantly more expensive than radar and have poorer all-weather performance due to their wavelength [2]. However, it has long been known that coherent samples over a large swath can be collected to *synthesize* a larger aperture size, thus improving the angular resolution attainable to a level commensurate with the wavelength and angle subtended by target as it crosses the antenna beamwidth; this technique has recently been rapidly gaining research interest in automotive applications due to these benefits [3]–[8].

Although automotive synthetic aperture radar (SAR) provides significant enhancement in angular resolution when compared with typical MIMO automotive radar, there are many advantages to integrating the data from multiple SAR

passes from different vehicles over time, shown in Fig. 1. One advantage is the ability to integrate out noise over time due to positional uncertainty, non-uniformity of sapling, and RF sensor noise resulting in an increased signal-to-noise ratio of $\sqrt{N}$ for the incoherent integration of N SAR images. Similarly, multiple passes afford multiple looks at the same objects which, if sampled at the same time by multiple vehicles at different viewing angles, such as in a spotlight mode, could provide higher resolution imagery, improving classification. Lastly, because the fusion of multiple SAR images inherently requires motion compensation and registration, the resultant translational vectors can be used as a separate odometry provider, or in the case of a metrology-grade reference image, a separate global localization provider; the latter may be especially useful in urban scenarios where high accuracy global navigation satellite system (GNSS) signals are not always available due to multi-path effects. Presently, there have been few works studying the fusion of multiple automotive SAR images from multiple platforms. One significant work the area of cooperative automotive SAR fusion was presented in [9] which focused on assessing the efficacy of coherent, and incoherent summation of multiple short SAR images over multiple passes of a vehicle using varying waveform bandwidths at $77\,\mathrm{GHz}$. This work showed favorable results using incoherent summation of waveforms due to the smooth rolloff of the main lobe, making it more tolerant to slight misalignment due to positional uncertainty. However, previous works have used sophisticated motion compensation techniques, such as time domain back projection, which require very high accuracy positional estimation of the platform to perform, and very high-power compute devices to perform image formation at near real time. While these provide very accurate representations of the imaging environment, they can be very computationally expensive when compared with simpler techniques, such as the Range Migration Algorithm (RMA), also known as the omega-k technique, which can be implemented using simple fast Fourier transforms on the range compressed data, assuming uniform spatial sampling [10]–[12]. Furthermore, high positional accuracy on the wavelength level may not always be available on consumer vehicles, and thus, other compensation techniques must be considered to compensate.

In this work, we expand upon our earlier work [13] showing low frequency polarimetric automotive SAR by presenting a simple multi-pass radar image fusion approach which compensates for non-uniform vehicle velocity over a large SAR image as a step towards distributed SAR image fusion. We demonstrate the incoherent fusion of multiple passes of the same scene, synthesizing images as if they were generated in a collaborative manner by multiple vehicles imaging the same scene sequentially, such as in a driving scenario. An efficient image formation algorithm is used with the assumption of uniform spatial sampling over the image swath, which creates along-track distortion due to the inherently nonlinear vehicle velocity; based on the assumption that the vehicle's velocity was quasi-static over small sub-sections of the aperture, the

images are coarsely aligned to a level commensurate with the image resolution using a two-dimensional sub-sample cross-correlation. Finally, the images are incoherently summed to provide the final fused result. This technique is demonstrated using data collected using the system described in [13] over three passes of various scenes at $5.9\,\mathrm{GHz}$ and shown for image alignment using the entire distorted scene, and the technique aligning sub-apertures, illustrating the relative improvement in performance.

II. IMAGE FORMATION

The image formation algorithm used in this work is the Range Migration Algorithm (RMA) [10]–[13]. In these experiments, the radar was configured to emit a linear frequency modulation (LFM) pulse for ranging at a constant pulse repetition frequency as the vehicle moved. The resultant received signal can be represented as the summation of all time-delayed copies of the LFM waveform scattered from the imaging environment at a given time t

$$s_{\mathrm{r}}(x_n,\, t) = \sum_i \alpha_i$$
$$\exp\left\{j2\pi\left[f_0\left(t - \tau_{\mathrm{d}}^{(i)}(x_n)\right) + \frac{K}{2}\left(t - \tau_{\mathrm{d}}^{(i)}(x_n)\right)^2\right]\right\} \quad (1)$$

where x_n is the position of the vehicle at the nth sample, f_0 is the carrier frequency, and $\tau_{\mathrm{d}}^{(i)}$ is the round-trip time-of-flight of the signal scattered from the ith scatterer in the scene; $K = \beta/\tau_{\mathrm{pd}}$ is the chirp-rate where β is the LFM bandwidth and τ_{pd} is the LFM pulse duration. For brevity we will focus on the single-scatterer case knowing that an actual scene is the linear summation of many scatterers. Following reception, the signal is dechirped using a hardware mixer to produce a baseband representation of the frequency which, written in terms of the target downrange and crossrange positions, y_{t} and x_{t}, respectively, is given by

$$s_{\mathrm{rd}}(x_n,\, t) =$$
$$\exp\left\{-j\frac{4\pi}{c}(f_0 + Kt)\sqrt{y_{\mathrm{t}}^2 + (x_{\mathrm{t}} - x_n)^2}\right\}. \quad (2)$$

The received waveform can then be Fourier transformed in the crossrange dimension along with a substitution of $k_r = \omega(t)/c = \frac{4\pi}{c}(f_0 + Kt)$ to obtain the image representation in the wavenumber domain, required to Stolt interpolation to map $\sqrt{k_r^2 - k_x^2} \rightarrow k_y$; a representation of the Fourier transform can be found using the principle of stationary phase

$$S(k_r,\, k_x) \approx \exp\left\{-jy_{\mathrm{t}}\sqrt{k_r^2 - k_x^2} - k_x x_{\mathrm{t}}\right\}. \quad (3)$$

After applying the interpolation, the image is focused yielding

$$S(k_y,\, k_x) = \exp\left\{j\left(y_{\mathrm{t}}k_y - k_x x_{\mathrm{t}}\right)\right\}. \quad (4)$$

which can be transformed back into the original spatial coordinates via a two-dimensional inverse Fourier transform producing

$$s(t,\, x_n) \approx \mathrm{sinc}\left\{\frac{ct - 2y_{\mathrm{t}}}{\rho_{\mathrm{R}}}\right\} \mathrm{sinc}\left\{\frac{2(x_n - x_{\mathrm{t}})}{\rho_{\mathrm{CR}}}\right\} \quad (5)$$
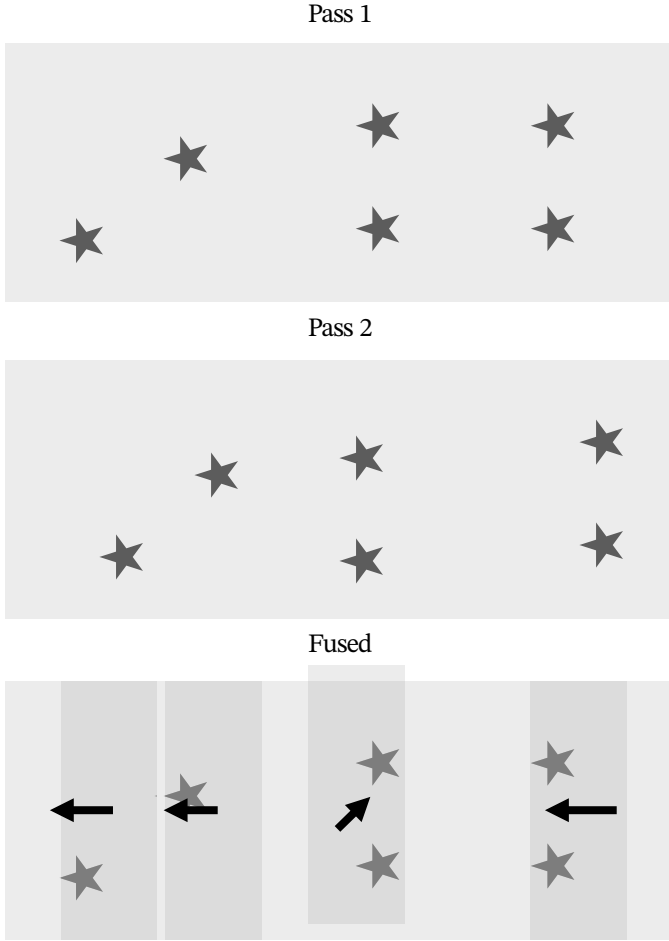
Pass 1

Pass 2

Fused

Fig. 2. Chunk based image registration technique. A single SAR image is used as the reference image, in this case Pass 1, to which all other images are registered. Small sub-sections of the image are aligned individually to compensate for motion non-linearities in the image formation, indicated by the black arrows in the Fused image.

where $\rho_R = c/(2\beta)$ is the downrange resolution and $\rho_{CR} = \lambda/2\theta_{3dB}$ where $\lambda = c/f_0$ and θ_{3dB} is the half-power beamwidth of the imaging system antennas [14].

III. IMAGE FUSION

The image fusion technique proposed here is a two-step process, shown pictorially in Fig. 2 and described in Algorithm 1, first separating the SAR image into smaller sub-aperture images wherein the velocity is assumed to be constant, then performing a two-dimensional cross-correlation of the image relative to a reference image. The reference image in this case may be an initial pass of the scene from one vehicle, or a metrology-grade SAR image of the scene from a high-definition SAR map, similar to traditional high-definition lidar maps used in automated vehicles (AVs) presently. Both techniques provide the ability to improve upon the localization of objects in the scene, as well as localization of the vehicle itself based on the registration correction vectors.

The first step of the separation of the SAR image involves finding a sub-aperture length over which the vehicle's speed

---

Algorithm 1: Image Fusion

Data: A list of 2-d matrices representing N SAR magnitude images in dB scale $\mathbf{F}_{SAR}$ of size $I \times J$ rows and columns, stride length δ, overlap ratio α

Result: Fused SAR image $\mathbf{Res}$

$\mathbf{Norm} \leftarrow \texttt{zeros}(I \times J)$;
/* Initialize $\mathbf{Res}$ to keyframe $\mathbf{F}_{SAR}[0]$ */
$\mathbf{Res} \leftarrow \mathbf{F}_{SAR}[0]$;
/* Iterate over each image */
for $k=1$ **to** $\texttt{len}(\mathbf{F}_{SAR})$ **do**
 /* Iterate over each sub-array of image */
 for $i=0$ **to** $\texttt{floor}(I/\delta)$ **do**
  $b \leftarrow i\delta$;   // start
  $c \leftarrow \delta(i+1)$;   // end
  $a \leftarrow \max[b - \delta\alpha, 0]$; // overlap left
  $d \leftarrow \min(c + \delta\alpha, I)$; // overlap right
  $\Delta_x, \Delta_y \leftarrow$
   $\texttt{xcorr}(\mathbf{F}_{SAR}[k][a:d], \mathbf{F}_{SAR}[0][a:d])$;
  $\mathbf{S} \leftarrow \texttt{translate}(\Delta_x, \Delta_y, \mathbf{F}_{SAR}[0][a:d])$
  $\mathbf{Res}[b:c] \leftarrow \mathbf{Res}[b:c] + \mathbf{S}[b-a:b-a+\delta]$;
  $\mathbf{Norm}[b:c] \leftarrow \mathbf{Norm}[b:c] +$
   $\texttt{where}(\mathbf{S}[b-a:b-a+\delta] > 0, 1, 0)$;
 $\mathbf{Res} \leftarrow \mathbf{Res}/\mathbf{Norm}$;

---

is quasi-static; in this work, a length of $\sim 24\,\mathrm{m}$ was used. This image is then used as the maximum allowable window size. A stride-length of less than the window size is then picked, in this case, a stride of $8\,\mathrm{m}$ was used. Thus, every sequential window of SAR data to be aligned was $24\,\mathrm{m}$ with 100% overlap of the previous and next sub-apertures used to improve registration.

The second step is the registration itself. An efficient two-dimensional cross-correlation method based on the nonlinear optimization and matrix-multiply discrete Fourier transform approach, described in [15]. The implementation found in the scikit-image python package [16], without normalization and an upsampling factor of $\kappa = 1000$ is used in this work.

IV. DATA COLLECTION

The data was collected at Michigan State University's Spartan Village AV research facility using the radar described in [13]; a system schematic is shown in Fig. 4 and picture of the full system is shown in Fig. 5. The radar utilized a single transmitter to generate a $200\,\mathrm{MHz}$ LFM at a carrier frequency of $5.9\,\mathrm{GHz}$ which was switched between vertically and horizontally polarized antennas. The scattered signals from the environment were simultaneously received on two receive channels using horizontally and vertically polarized antennas and coherently dechirped by mixing the received signal with the transmitted waveform to obtain fully polarimetric baseband information, however, in this paper, only the co-polarized

Fig. 3. Ground-based image of the scene imaged. Corner reflector can be seen in the center of the image near the vehicle, slightly behind the row of trees. Other features of interest include small steps in front of the apartment building, as well as the vertical pillars on the balcony of the apartment building.
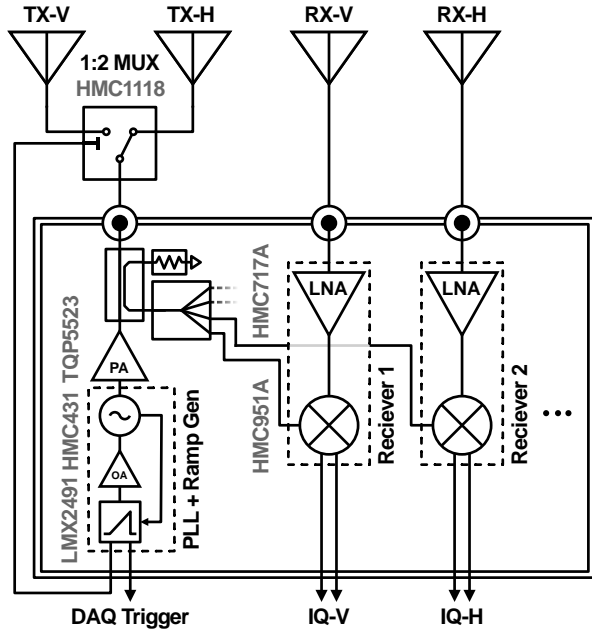

Fig. 4. Radar system schematic. Transmitter polarization was selected using a 1:2 mux while co- and cross-polarization scatters were simultaneously received. A USB DAQ was used to simultaneously sample and digitize both received signals to be stored and processed on a computer.
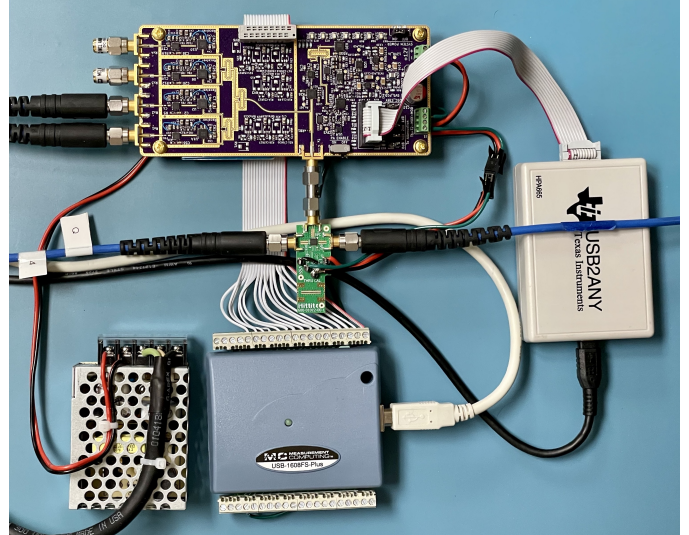

Fig. 5. Photograph of the radar hardware used in this experiment. The radar PCB is shown on top with the transmit/receive switch in the center and DAQ on the bottom. The lower-left shows the power supply, and the right shows the radar programmer.

V. EXPERIMENTAL RESULTS

Experimental results using this technique are presented in Figs. 6 and 7. In Fig 6, two regions of interest (ROIs) are highlighted in yellow to highlight areas of improved image registration using the sub-section alignment technique. In this experiment, an apartment building was imaged with several trees and a corner reflector (in ROI 2 at the far right, aligned with the row of trees) in front of the building. The optical image in Fig. 7 is shown without foliage on the trees to show ground detail, however the experiment was run with foliage on the trees. The SAR images were taken in two different passes of the vehicle, simulating a system where multiple vehicles may pass the same scene and fuse their images together to improve spatial diversity and angular resolution. Each of the scenes was formed with the assumption of constant vehicle velocity, however the true vehicle velocity deviated during the image pass; an example of the velocity deviation is shown in the optical image Fig. 7. This deviation creates distortion in the images causing issues when aligning the full SAR

images are considered. These signals were then sampled at $100\,\mathrm{kSa/s}$ using a Measurement Computing USB1608-FS+ DAQ and saved on a computer for post-processing.

The vehicle used for collecting the data was the Michigan State University CANVAS Chevrolet Bolt AV, shown in Fig. 3. The vehicle had two 13.2 dBi Yagi-Uda antennas used for transmitting near the rear of the roof rack and two 9.5 dBi bi-quad antennas used for reception near the front of the roof rack. Additionally, the vehicle utilized real-time kinematic GNSS to obtain a positional estimate of $< 2.5\,\mathrm{cm}$ used for mapping the trajectory during the SAR passes. However, for the image formation, a linear, constant velocity was assumed. Based on the signal bandwidth, carrier frequency, and antenna beamwidth, the theoretical resolution of the system was $\rho_{\mathrm{R}} = 0.75\,\mathrm{m}$ and $\rho_{\mathrm{CR}} = 3.7\,\mathrm{cm}$.
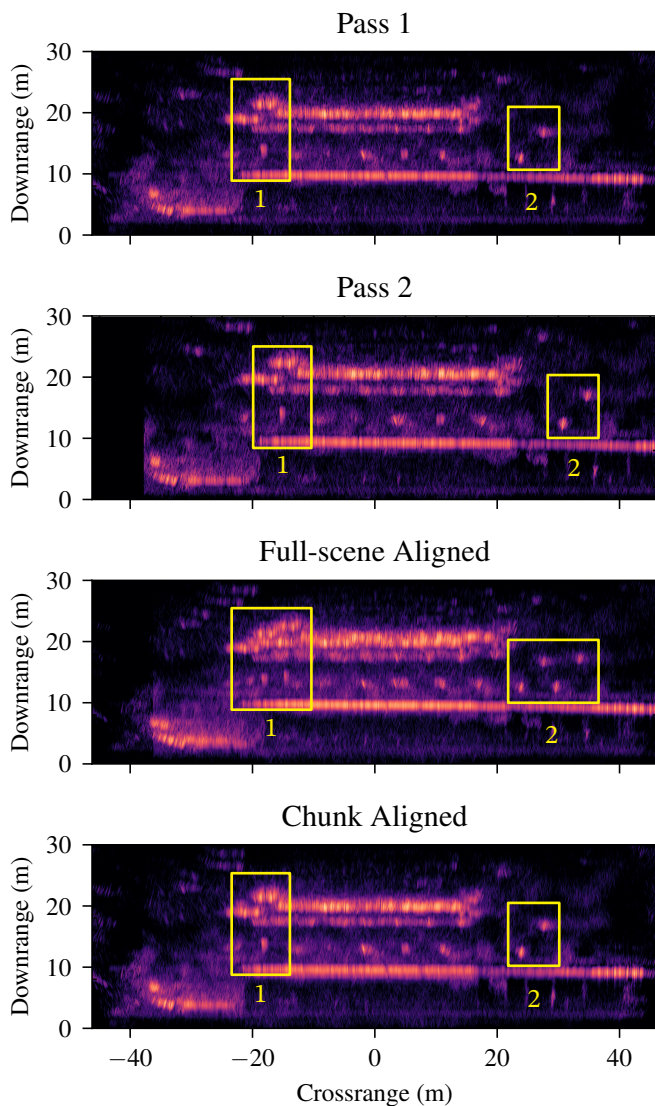
Fig. 6. Horizontally polarized (HH) synthetic aperture images of the scene. Pass 1 and Pass 2 are shown at the top followed by the full-scene aligned image and the chunk aligned scene. The chunk alignment method shows clear improvements in image clarity while the full-scene aligned image shows double images due to misalignment of features over the large swath from vehicle speed variation between passes. Two ROIs are highlighted in yellow to clearly show the improvement in image registration and fusion of the proposed technique.
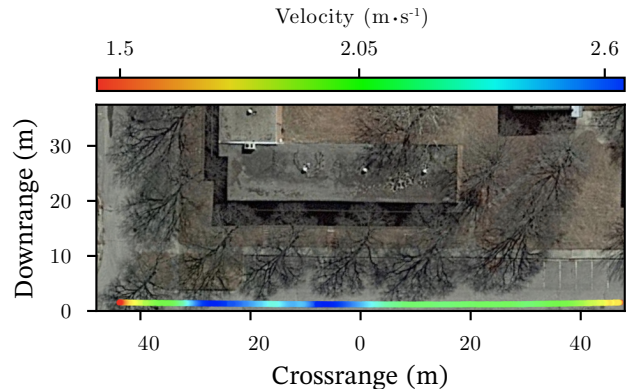

Fig. 7. Optical satellite image of the scene; SAR data was collected with foliage on trees, however optical image is shown without foliage to improve visibility of ground features. Vehicle trajectory and velocity from Pass 1 is plotted at the bottom to illustrate velocity variation.
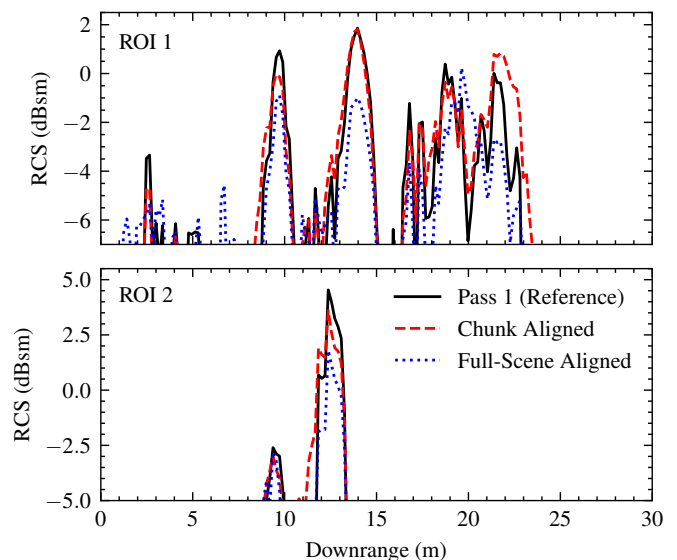

Fig. 8. Downrange cross-sections of (top) ROIs 1 and 2 at a crossranges of -18.94 m and 23.47 m, respectively. In ROI 1 the large scatterers at 10 m and 13 m downrange are due to the parking lot curb and a tree trunk. Distributed scatterers from 18–23 m are due to the balcony and opening into building. In ROI 2, the parking curb and corner reflector at are shown at 9 m and 13 m respectively. A $\sim$3 dB loss is observed in the "Full-Scene Align" results in areas of strong scatterers due to poor alignment of the images. Also note that the "Chunk Aligned" slice is smoother than the "Pass 1 (Reference)" slice.

image as is shown in the Full-Scene Aligned image in Fig. 6, especially present in ROIs 1 where the recess into the building is completely obscured and ROI 2 where ghost targets appear. To mitigate these artifacts the chunk alignment technique described in this paper is applied, shown in the Chunk Aligned image in Fig. 6 which shows good alignment of the features in ROIs 1 and 2 once again. Examples of downrange slices in ROIs 1 and 2 are shown in Figs. 8. In the downrange slices the $\sim$3 dB loss due to misalignment of strong scatterers is seen in both ROIs for the full-scene aligned image; furthermore a smoothing can be seen in the "Chunk Aligned" slice due to the added information from multiple boservations of the scene.

Using this technique which efficiently aligns sub-images in the full SAR it can be clearly seen that the features can be re-aligned, providing an improvement in image clarity over each of the individual images using a relatively simple algorithm.

VI. CONCLUSION

In this paper, a simple and efficient technique for the registration and fusion of multi-pass SAR images is presented. Based on the experimental results, a clear improvement in the overall formed SAR image is seen.

REFERENCES

[1] On-Road Automated Driving (ORAD) Committee, *Taxonomy and Definitions for Terms Related to Driving Automation Systems for On-Road Motor Vehicles*, Jun 2018.

[2] M. Jokela, M. Kutila, and P. Pyykönen, "Testing and validation of automotive point-cloud sensors in adverse weather conditions," *Applied Sciences*, vol. 9, no. 11, p. 2341, 2019.

[3] H. Iqbal, M. B. Sajjad, M. Mueller, and C. Waldschmidt, "Sar imaging in an automotive scenario," in *2015 IEEE 15th Mediterranean microwave symposium (MMS)*. IEEE, 2015, pp. 1–4.

[4] R. Feger, A. Haderer, and A. Stelzer, "Experimental verification of a 77-ghz synthetic aperture radar system for automotive applications," in *2017 IEEE MTT-S International Conference on Microwaves for Intelligent Mobility (ICMIM)*. IEEE, 2017, pp. 111–114.

[5] A. Laribi, M. Hahn, J. Dickmann, and C. Waldschmidt, "Performance investigation of automotive sar imaging," in *2018 IEEE MTT-S International Conference on Microwaves for Intelligent Mobility (ICMIM)*. IEEE, 2018, pp. 1–4.

[6] M. Steiner, T. Grebner, and C. Waldschmidt, "Millimeter-wave sar-imaging with radar networks based on radar self-localization," *IEEE Transactions on Microwave Theory and Techniques*, vol. 68, no. 11, pp. 4652–4661, 2020.

[7] D. Tagliaferri, M. Rizzi, M. Nicoli, S. Tebaldini, I. Russo, A. V. Monti-Guarnieri, C. M. Prati, and U. Spagnolini, "Navigation-aided automotive sar for high-resolution imaging of driving environments," *IEEE Access*, vol. 9, pp. 35 599–35 615, 2021.

[8] M. Farhadi, R. Feger, J. Fink, T. Wagner, and A. Stelzer, "Automotive synthetic aperture radar imaging using tdm-mimo," in *2021 IEEE Radar Conference (RadarConf21)*. IEEE, 2021, pp. 1–6.

[9] D. Tagliaferri, M. Rizzi, S. Tebaldini, M. Nicoli, I. Russo, C. Mazzucco, A. V. Monti-Guarnieri, C. M. Prati, and U. Spagnolini, "Cooperative synthetic aperture radar in an urban connected car scenario," in *2021 1st IEEE International Online Symposium on Joint Communications & Sensing (JC&S)*. IEEE, 2021, pp. 1–4.

[10] C. Cafforio, C. Prati, and F. Rocca, "Sar data focusing using seismic migration techniques," *IEEE transactions on aerospace and electronic systems*, vol. 27, no. 2, pp. 194–207, 1991.

[11] W. Melvin and J. Scheer, *Principles of Modern Radar: Advanced Techniques, Volume 2*, ser. EBSCO ebook academic collection. Institution of Engineering and Technology, 2012.

[12] E. Jansing, *Introduction to Synthetic Aperture Radar: Concepts and Practice*. McGraw-Hill Education, 2021.

[13] J. M. Merlo and J. A. Nanzer, "A c-band fully polarimetric automotive synthetic aperture radar," *IEEE Transactions on Vehicular Technology*, vol. 71, no. 3, pp. 2587–2600, 2022.

[14] M. Richards, W. Holm, and J. Scheer, *Principles of Modern Radar: Basic Principles, Volume 1*, ser. Electromagnetics and Radar. Institution of Engineering and Technology, 2010.

[15] M. Guizar-Sicairos, S. T. Thurman, and J. R. Fienup, "Efficient subpixel image registration algorithms," *Opt. Lett.*, vol. 33, no. 2, pp. 156–158, Jan 2008. [Online]. Available: https://opg.optica.org/ol/abstract.cfm?URI=ol-33-2-156

[16] S. van der Walt, J. L. Schönberger, J. Nunez-Iglesias, F. Boulogne, J. D. Warner, N. Yager, E. Gouillart, T. Yu, and the scikit-image contributors, "scikit-image: image processing in Python," *PeerJ*, vol. 2, p. e453, 6 2014. [Online]. Available: https://doi.org/10.7717/peerj.453